JACS
JOURNAL OF THE AMERICAN CHEMICAL SOCIETY
Article
pubs.acs.org/JACS

# An Organometallic Building Block Approach To Produce a Multidecker 4*f* Single-Molecule Magnet

Jennifer J. Le Roy,[†] Matthew Jeletic,[†] Serge I. Gorelsky,[†] Ilia Korobkov,[†] Liviu Ungur,[‡] Liviu F. Chibotaru,[‡] and Muralee Murugesu*,[†]

[†]Chemistry Department and the Centre for Catalysis Research and Innovation, University of Ottawa, 10 Marie Curie, Ottawa, Ontario K1N 6N5, Canada

[‡]Division of Quantum and Physical Chemistry and INPAC Institute for Nanoscale Physics and Chemistry, Katholieke Universiteit Leuven, Celestijnenlaan, 200F, 3001, Belgium

*Supporting Information*

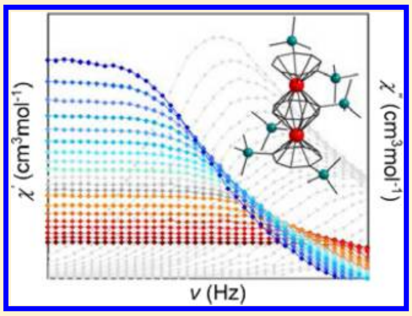

**ABSTRACT:** An organometallic building block strategy was employed to investigate the magnetic properties of a $Ln^{III}$ organometallic single-ion magnet (SIM) and subsequent single-molecule magnet (SMM) after coupling two of the monomeric units. New homoleptic $Dy^{III}COT''_2$ and $Ln^{III}_2COT''_3$ (Ln = Gd, Dy) complexes have been synthesized. DFT calculations of the bimetallic $Dy^{III}$ complex indicate strong metal−ligand covalency and uneven donation to the $Dy^{III}$ ions by the terminal and internal $COT''^{2-}$ (cyclooctatetraenide) rings that correlate with the respective bond distances. Interestingly, the studies also point to a weak covalent interaction between the metal centers, despite a large separation. The ac susceptibility data indicates that both $Dy^{III}COT''_2$ and $Dy^{III}_2COT''_3$ act as an SIM and an SMM, respectively, with complex multiple relaxation mechanisms. Ab initio calculations reveal the direction of the magnetic anisotropic axis is not perpendicular to the planar COT″ rings for both $Dy^{III}COT''_2$ and $Dy^{III}_2COT''_3$ complexes due to the presence of trimethylsilyl groups on the COT″ rings. If these bulky groups are removed, the calculations predict reorientation of the anisotropic axis can be achieved.

## 1. INTRODUCTION

Single metal centers potentially act as magnets when their spins are coupled with large intrinsic magnetic anisotropy. When this magnet-like behavior is intrinsic to the molecule, such molecules are termed single-molecule magnets (SMMs)[1] or single-ion magnets (SIMs).[2]

Although lanthanide SIMs are fashionable due to large intrinsic magnetic anisotropy, they still fail to surpass the record blocking temperature set by polynuclear SMMs.[3] This is still valid for both polynuclear transition metal and lanthanide SMMs. Theoretically speaking, larger barriers are expected for polynuclear complexes as they possess many spin carriers and when coupled ferromagnetically could lead to a large spin ground state. Controlling the spins has been achieved in transition metal complexes;[4] however, controlling the magnetic anisotropy remains a difficult challenge. Unlike in most transition metal ions, lanthanides possess large intrinsic magnetic anisotropy, but their core 4*f* orbitals minimally participate in exchange interactions. As a result, the large barriers are often attributable to single-ion behavior. If large barriers are required for technological applications, then single-ion anisotropy combined with the limited spin of the single metal center is not sufficient. Thus, inducing significant interactions between highly anisotropic lanthanide centers is vital. Long, Evans, and co-workers recently induced significant interaction between two $Ln^{III}$ ions by coupling them via an $N_2$ radical, and this subsequently led to the record blocking temperature to date.[3c] Although this is quite a unique result, stabilizing such systems for larger molecules is difficult. Therefore, promoting efficient coupling between lanthanide ions requires a new synthetic approach to isolate these molecules.

Synthetic strategies to date for isolating polynuclear SMMs mainly take advantage of coordination chemistry. More specifically, two main synthetic approaches predominate: (1) serendipitous approach[1a,4,5] and (2) rational building block approach.[6] Although the former method prevails as much more fruitful in isolating large numbers of SMMs, the latter offers better control and fine-tuning of the molecular architecture and magnetic properties.

These methods greatly advanced the field of SMMs, and yet an underlying problem still exists; oxygen and nitrogen bridged coordination complexes have limited orbital overlap with the shielded 4f orbitals. In an effort to couple and induce significant spin interactions, we have turned our attention toward organometallic complexes where metal centers are bridged by large aromatic cyclooctatetraenide ($COT^{2-}$) rings. Therefore, taking advantage of the $\pi$ electron cloud created by the multiple $sp^2$ carbon atoms may facilitate efficient overlap with the metal *f* orbitals, subsequently leading to non-negligible interactions. With this in mind, we have chosen to investigate lanthanide

**Received:** November 1, 2012
**Published:** February 7, 2013

cyclooctatetraenide ($COT^{2-}$) sandwich complexes as building blocks to construct polynuclear SMMs. Herein, we report the charged building block $[Dy^{III}(COT'')_2]Li(DME)_3$, **1**, a unique example of a COT-based organopolylanthanide SMM, $[Dy^{III}{}_2(COT'')_3]$, **2**, and its $Gd^{III}$ analogue, $[Gd^{III}{}_2(COT'')_3]$, **3**.

## 2. EXPERIMENTAL SECTION

**2.1. General Considerations.** Unless specified otherwise, all manipulations were performed under an inert atmosphere using standard Schlenk or glovebox techniques. Glassware was oven-dried before use. Hexanes, toluene, tetrahydrofuran (THF), and dimethoxyethane (DME) were dried using activated alumina. Dry, air-free cyclopentane was purchased from Acros Organics and used as is. All chemicals were purchased from Thermofisher Scientific or Strem Chemicals and used without further purification. The $[Li_4(COT'')_2(THF)_4]$ was synthesized using a previously published procedure.[7]

**2.2. Synthesis of Complexes 1−3.** To a 20 mL scintillation vial were added $DyCl_3$ (0.823 g, 3.06 mmol) and $[Li_4(COT'')_2(THF)_4]$[7] (3.617 g, 4.54 mmol). The reagents were then stirred for 5 min before 3 mL of DME was added. The solution was stirred at room temperature, and after 36 h the precipitate (LiCl) was filtered off through a fine fritted funnel containing Celite. Large orange block crystals were grown from a concentrated solution (1:1 DME:hexanes) providing $[Dy^{III}(COT'')_2]Li(DME)_3$, **1**, in 57% yield. Isolated crystals are extremely air sensitive. Anal. Calcd for $C_{40}H_{78}DyLiO_6Si_4$: C, 51.28; H, 8.39. Found: C, 51.19; H, 8.03. Selected IR data for **1** ($cm^{-1}$): 2954 (br), 2892 (m), 1590 (w), 1447 (w), 1404 (w), 1247 (s), 1051 (s), 982 (w), 933 (m), 839 (s), 749 (m), 720 (m), 678 (w), 651 (w), 635 (w).

Complex **2** was produced from a reaction of $[Dy^{III}COT''_2]Li(THF)_4$[8] (0.200 g, 0.195 mmol) with $CoCl_2$ (0.013 g, 0.0976 mmol). The reagents were stirred in 5 mL of toluene for 24 h, and refluxed for an additional 5 h. $Co^0$ was filtered off as a black precipitate. The remaining solution was concentrated to an amber oil where large block crystals of $[Dy^{III}{}_2(COT'')_3]$, **2**, were grown by the addition of cyclopentane at −35 °C with 25% yield. Individual block crystals were picked out of the oil and washed thoroughly with cold cyclopentane. Isolated crystals are extremely air sensitive. Anal. Calcd for $C_{42}H_{72}Dy_2Si_6$: C, 47.12; H, 6.78. Found: C, 47.35; H, 6.70. Selected IR data for **2** ($cm^{-1}$): 2999 (w), 2957 (br), 2900 (m) 1450 (br), 1403 (w), 1247 (s), 1049 (m), 978 (w), 933 (w), 837 (s), 748 (m), 721 (w), 688 (w), 634 (w).

Complex **3** was produced in an analogous manor to **2** where $[Gd^{III}COT''_2]Li(THF)_4$ (0.167 g, 0.164 mmol) and $CoCl_2$ (0.011 g, 0.0819 mmol) in 5 mL of toluene was stirred for 24 h, and refluxed for an additional 5 h. $Co^0$ was filtered off as a black precipitate. The remaining solution was concentrated to an amber oil where large orange block crystals were grown by the addition of cyclopentane at −35 °C with 30% yield. Block crystals were removed and washed thoroughly with cold cyclopentane. Isolated crystals are extremely air sensitive. Anal. Calcd: C, 47.59; H, 6.85. Found: C, 47.31; H, 6.52. Selected IR data for **3** ($cm^{-1}$): 3031 (w), 2967 (br), 2895 (m), 1459 (br), 1400 (m), 1247(s), 1052 (s), 983 (m), 936 (w), 837 (br), 753 (w), 726 (w), 681 (w), 638 (m).

**2.3. X-ray Crystallography.** Single crystals of **1** were grown from a concentrated solution of 1:1 DME:hexanes. Large orange block crystals were additionally washed with hexanes. Single crystals of **2**−**3** were grown from a concentrated toluene solution at −35 °C with the addition of cyclopentane. Large block crystals were thoroughly washed with cold cyclopentane. For each **1**−**3**, a suitable prism shaped crystal was mounted in inert oil and transferred to the cold gas stream of the diffractometer. Unit cell measurements and intensity data were collected at 200 K on a Bruker-AXS SMART 1 k CCD diffractometer using graphite monochromated $MoK_\alpha$ radiation ($\lambda$ = 0.71073 Å). The data reduction included a correction for Lorentz and polarization effects, with an applied multiscan absorption correction (SADABS).[9] The crystal structure was solved and refined using the SHELXTL[10] program suite. Direct methods yielded all non-hydrogen atoms, which were refined with anisotropic thermal parameters. All hydrogen atom positions were calculated geometrically and were riding on their respective atoms.

**2.4. Magnetic Measurements.** The magnetic susceptibility measurements for **1**−**3** were obtained using a Quantum Design SQUID magnetometer MPMS-XL7 operating between 1.8 and 300 K for dc applied fields ranging from −7 to 7 T. The dc analyses were performed on polycrystalline samples wrapped in a polyethylene membrane (prepared in an inert atmosphere) under a field ranging from 0 to 7 T between 1.8 and 300 K. The ac susceptibility measurements were carried out under an oscillating ac field of 3 Oe and ac frequencies ranging from 1 to 1500 Hz and dc fields ranging from 0 to 1600 Oe. Magnetization data were collected at 100 K to check for ferromagnetic impurities that were absent in all samples. Diamagnetic corrections were applied for the sample holder and the core diamagnetism from the sample (estimated with Pascal constants).

**2.5. Electronic Structure Calculations.** Density functional theory (DFT) calculations were carried out with the Gaussian 09 software (revision A.02)[11] using the spin-unrestricted molecular orbital formalism. Crystal structure geometry in which the silyl groups were replaced by protons and all C−H bond distances were adjusted from the X-ray model values to 1.07 Å was used in single-point calculations. The broken-symmetry (BS)[12] singlet wave function was constructed from the optimized wave functions of two $Dy^{III}(COT'')$ fragments and the central COT″ dianionic ligand using the AOMix software.[13] The triple-$\zeta$ TZVP basis set[14] for C and H atoms and the SDD basis set and effective core potential[15] for $Dy^{III}$ were used. The calculations employed the B3LYP exchange-correlation functional.[16] The wave function stability checks were performed to make sure that the calculated wave function corresponds to the electronic ground state (the stable keyword in Gaussian). Atomic spin densities, charges, Mayer bond orders,[17] orbital compositions, and changes in fragment orbital populations[18] were calculated using the AOMix software[3] and the Mulliken population analysis (MPA).[19] The electronic energy of the ferromagnetically coupled state of the complex was also calculated. Its energy is 1.2 kcal $mol^{-1}$ higher than the energy of the BS singlet state.

**2.6. CASSCF Calculations.** All ab initio calculations were performed using the MOLCAS 7.6. program package and were of CASSCF/RASSI/SINGLE_ANISO level of theory. In the smallest structural fragment, all silyl groups were replaced by hydrogens at a fixed distance of 1.07 Å. In the medium fragment, the methyl groups were replaced by H, thus preserving the Si atoms in the calculation, while in the largest computational fragment, the entire molecule was kept as is. The neighboring $Dy^{III}$ ion was computationally substituted by the diamagnetic $Lu^{III}$ ion. Two basis sets, both taken from the ANO-RCC basis set library, were employed for computation of the above structural models: basis **1** − small and basis **2** − large. Contractions of the employed basis sets are provided in Table S1. As a result, we have the following computational models: A1, A2, B1, B2, C1, and C2. The active space of the complete active space self-consistent field CASSCF method, denoted AS1, included nine electrons spanning seven orbitals from the 4*f* shell of the $Dy^{III}$ ion. The spin−orbit coupling was computed by mixing all (21) spin sextet states, 128 out of 224 spin quartet states and 130 out of 490 spin doublet states. Table S2 shows the obtained spin−orbit energies and the *g* tensors in the lowest Kramers doublets for these computational models.

## 3. RESULTS AND DISCUSSION

**3.1. Synthesis.** To isolate sandwich type molecules, the use of planar cyclooctatetraenide ($COT^{2-}$) ligands has become a convenient synthetic procedure.[20] For example, we recently reported an organolanthanide sandwich complex, $[Dy^{III}(COT'')_2Li(THF)(DME)]$,[8] using soluble 1,4-bis(trimethylsilyl)cyclooctatetraenyl dianion (COT″) derivative where the Li atom is bound to the COT″ ring yielding an asymmetric molecule. Using similar methodology but with replacing THF with DME, the mononuclear complex, $[Dy^{III}(COT'')_2]Li(DME)_3$, **1**, was obtained. Recrystallizing **1** from a concentrated solution of 1:1 DME:hexanes generates large, vibrant orange blocks suitable for X-ray diffraction. In our experiments, we found that the presence of DME on the molecule aids in growing large crystals suitable for X-ray diffraction, whereas when THF is employed as the primary solvent, fine needle shaped crystals can be isolated. The latter crystals are too small for single crystal X-ray diffraction.

Our strategy for designing organopolymetallic SMMs is inspired from Edelmann and co-worker's methodology.[21] The strategy consists of a building block approach whereby **2** is built from the bottom up. The monometallic sandwich complex, $[Dy^{III}COT''_2]^-$,[8] can be isolated from the planar $COT''^{2-}$ ligands. The isolated complex is an ideal charged building block where oxidizing the ligand leads to coupling of the monomer units resulting in complex **2**. In the isolated dinuclear complex, a central COT″ ring bridges both metal centers, thus providing an ideal delocalized superexchange pathway for magnetic interactions. Reaction of 2 equiv of $[Dy^{III}COT''_2]Li(THF)_4$[8] with 1 equiv of $CoCl_2$ generates **2**, along with an 1 equiv of 1,4-bis(trimethylsilyl) cyclooctatetraene, 1 equiv of LiCl, and $Co^0$ metal (Scheme 1). The synthetic strategy for complex **3** is analogous to **2** where 2 equiv of $[Gd^{III}COT''_2]Li(THF)_4$[8] combined with 1.5 equiv of $CoCl_2$ generates **3**. The isostructurality and common oxidation states of lanthanide ions prove to be useful in the isolation of analogous compounds of the lanthanide series using the same synthetic methodology.

**Scheme 1. Synthetic Route to the $Dy^{III}$ Homoleptic Triple-Decker Sandwich Complex $[Dy^{III}_2(COT'')_3]$, Starting from 1,5-Cyclooctadiene**

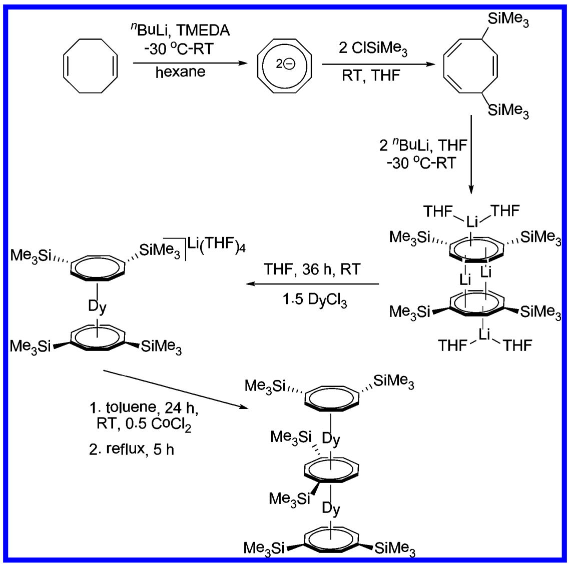

**3.2. Structural Characterization.** The single-crystal X-ray crystallography studies reveal that **1** crystallizes in triclinic $P\bar{1}$ space group. Figure 1, top, displays the molecular structure of **1**, and comprises two silylated $COT''^{2-}$ ligands that bound $\eta^8$ to the central $Dy^{III}$ ion. In the crystal lattice, the lithium counterion adopts an octahedral coordination environment filled by three 1,2-dimethoxyethane (DME) molecules (Figures S1−S3). The shortest $Li-C_{COT''}$ distance is 5.62 Å and is more than double that in $[Dy^{III}(COT'')_2Li(THF)(DME)]$[8] (2.33−2.51 Å), supporting that the lithium is not bound to the COT″ ring. In contrast to $[Dy^{III}(COT'')_2Li(THF)(DME)]$,[8] the two $Ln^{III}-COT''_{centroid}$ distances are identical (1.90 Å) as a result of induced symmetry by the lithium not binding to the COT″ ring. The average $Dy^{III}-C_{COT''}$ distance is 2.66 Å and is comparable to the $Dy^{III}-C_{COT''}$ bond distance (2.67 Å) in $[Dy^{III}(COT'')_2Li(THF)(DME)]$. The closest intermolecular

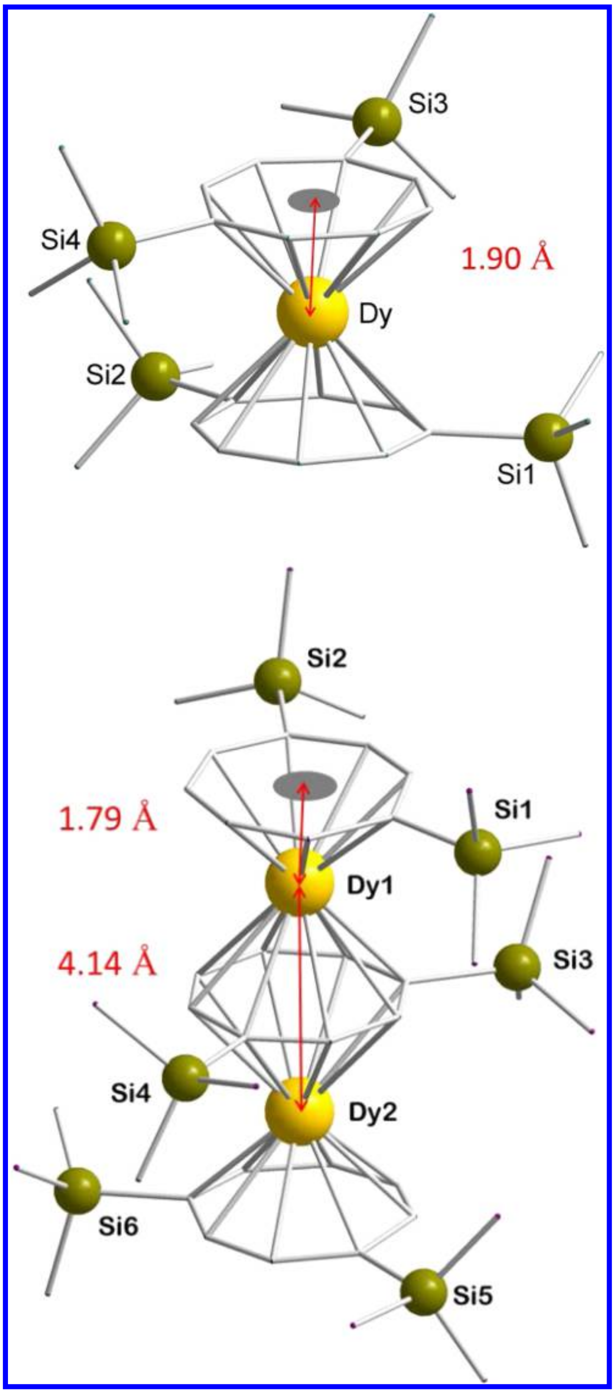

**Figure 1.** Partially labeled X-ray structures of **1** (top) and **2** (bottom) with H atoms omitted for clarity. Yellow (Dy), gray (C), green (Si). Dy···COT″ inner centroid distance of 1.90 Å for **1**. Dy···Dy distance of 4.14 Å, Dy···COT″ outer centroid distance of 1.79 Å, Dy···COT″ inner centroid distance of 2.07 Å for **2**.

Dy$^{\mathrm{III}}\cdots$Dy$^{\mathrm{III}}$ distance is 10.39 Å; therefore, intermolecular magnetic interactions should be negligible (Figures S1–S3).

Complex **2** crystallizes in a tetragonal $I\bar{4}$ space group, where the unit cell is composed of four dinuclear triple-decker units. The neutral molecular unit is a homoleptic triple-decker sandwich complex containing two Dy$^{\mathrm{III}}$ centers that bind to opposing sides of the COT″ rings (Figure 1, bottom). The outer COT″ ligands coordinate in $\eta^8$ manner to Dy$^{\mathrm{III}}$ ions with Dy$^{\mathrm{III}}$–C bond distances ranging from 2.54 to 2.62 Å, whereas the central ring serves as $\mu$-$\eta^8$:$\eta^8$ bridging ligand with a Dy$^{\mathrm{III}}$–C bond distance range of 2.73–2.79 Å. The Dy$^{\mathrm{III}}\cdots$Dy$^{\mathrm{III}}$ distance is 4.14 Å. The distance between the outer COT″ centroid and Dy$^{\mathrm{III}}$ ion is 1.79 Å, whereas the inner COT″centroid–Dy$^{\mathrm{III}}$ distance is significantly longer (2.07 Å). This differs from **1** where a more symmetrical arrangement was observed with an average COT″centroid–Dy$^{\mathrm{III}}$ distance of 1.90 Å. The reasons for this will be discussed in the computational section (vide infra).

The outer COT″ rings are in near parallel arrangement with the central ring with a slight tilt angle of 1.86° (Figure S4), and the angle between the three COT″ centroids is 177.4°. The presence of silyl groups most likely distorts the structure from a perfect parallel arrangement. Such near parallel arrangement of rings is rare in multinuclear organolanthanide chemistry.[22] Also of interest, when viewing the structure of **1**, **2** and **3** from above the carbon atoms in each layer are staggered with C atoms in other layers. This is most likely dictated by the sterics of the bulky silyl groups, but specific orbital coordination arrangements around the central Dy$^{\mathrm{III}}$ ion could also influence this arrangement (Figures S5, S6). Close inspection of the packing arrangement of **2** reveals the closest intermolecular Dy$^{\mathrm{III}}\cdots$Dy$^{\mathrm{III}}$ distance is 9.2 Å and the complex packs orthogonal with respect to itself in the previous layer (Figures S7–S9). Overall complex **2** is structurally analogous to the previously reported Nd complex as well as **3**.[21e] For simplicity, the molecular structure of **3** is located in the Supporting Information as well as a table containing the structural details of **1**–**3** (Table S5, Figures S10–S13).

**3.3. Electronic Structure of 2.** To probe the electronic structure of complex **2**, DFT calculations at the spin-unrestricted B3LYP[16]/TZVP[14] level (the SDD[15] basis set and effective core potential for Dy$^{\mathrm{III}}$) were conducted using the crystal structure geometry. The silyl groups were replaced by protons, and all C–H bond distances were adjusted from the X-ray model values to 1.07 Å to simplify the calculations while still providing an accurate bonding picture. The optimized wave functions of two Dy$^{\mathrm{III}}$(COT″) fragments and the central COT″ ligand allowed for construction of the BS singlet wave function. The bonding contributions in the triple decker sandwich complex were evaluated with the optimized wave function for the BS singlet state. Figure 2 displays the spin density of the BS singlet where each Dy$^{\mathrm{III}}$ atom carries a spin density of 5.57 au attributable to the five singly occupied 4*f* orbitals on Dy$^{\mathrm{III}}$. In contrast, the terminal COT″ ligands demonstrate significant spin polarization (a spin density of 0.39 au of the opposite sign to the neighboring Dy atom). These observations are in line with the results obtained for the mononuclear $[\mathrm{Dy^{III}COT''_2}]^-$ complex.[8]

In the triple decker sandwich complex, each Dy$^{\mathrm{III}}$ ion interacts with the terminal and the central COT″ ligands. The net charges of the terminal and central COT″ ligands are −0.30 and −0.12 au, respectively. These charges indicate that the terminal dianionic COT″ ligands donate 1.70 e$^-$ to each Dy$^{\mathrm{III}}$ ion. The central dianionic COT″ ligand donates larger electron density to the Dy$^{\mathrm{III}}$ ions (1.88 e$^-$), but because there are two Dy$^{\mathrm{III}}$ ions, each receives only 0.94 e$^-$. The Mayer bond orders[17] for the stronger Dy$^{\mathrm{III}}$-ligand interactions (2.3 for the interaction with the terminal COT″ and 1.2 for the interaction with the central COT″) confirm this. Thus, stronger terminal COT″→Dy$^{\mathrm{III}}$ charge donation explains the shorter Dy$^{\mathrm{III}}$–C$_{\mathrm{centroid}}$ distances for the terminal COT″–Dy$^{\mathrm{III}}$ fragment. The analysis of the wave function in terms of contributions from fragment orbitals indicates that only charge donation from the COT″ ligands to Dy$^{\mathrm{III}}$ contributes to the covalent bonding in this complex. Eight occupied orbitals of the central COT″ dianionic ligand participate significantly (change in orbital population is greater than 3%) in covalent bonding with the two Dy$^{\mathrm{III}}$ ions (Figure S14). Most of the donated electron density comes from four $\pi$ orbitals (HOMO, HOMO−1, HOMO−2, and HOMO−3). Thus, the whole superexchange interaction via the central COT″ ligand plays a major role in defining the spin interaction between the two Dy$^{\mathrm{III}}$ ions. There is also a weak direct Dy$^{\mathrm{III}}$–Dy$^{\mathrm{III}}$ covalent interaction with the bond order of 0.04. Although this value is relatively small, it is still surprising to observe such direct Dy$^{\mathrm{III}}$–Dy$^{\mathrm{III}}$ covalent interaction. Further spectroscopic studies are currently underway to validate this interaction.

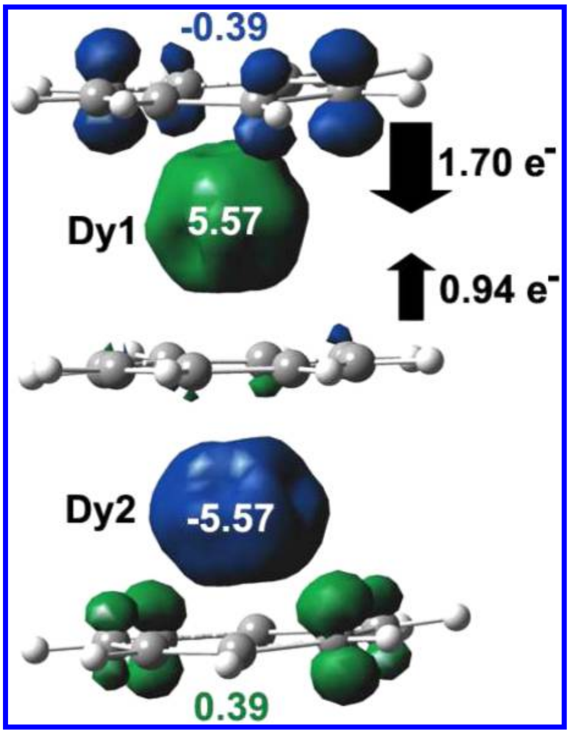

**Figure 2.** Spin density distribution of the BS singlet state of **2**. Green and blue indicate the regions of positive and negative spin densities, respectively. Black arrows indicate charge donation from the dianionic COT″ ligands to Dy$^{\mathrm{III}}$ ions.

**3.4. Magnetic Properties of 1, 2, and 3.** To probe the magnetic properties of all three compounds, magnetic susceptibilities were measured on freshly prepared polycrystalline samples (under nitrogen) with a SQUID magnetometer. Direct current (dc) magnetic susceptibility measurements were performed in the temperature range of 1.8–300 K under an applied dc field of 1000 Oe (Figure 3). The room temperature $\chi T$ value of 14.10 cm$^3$ K mol$^{-1}$ for **1** is in agreement with the

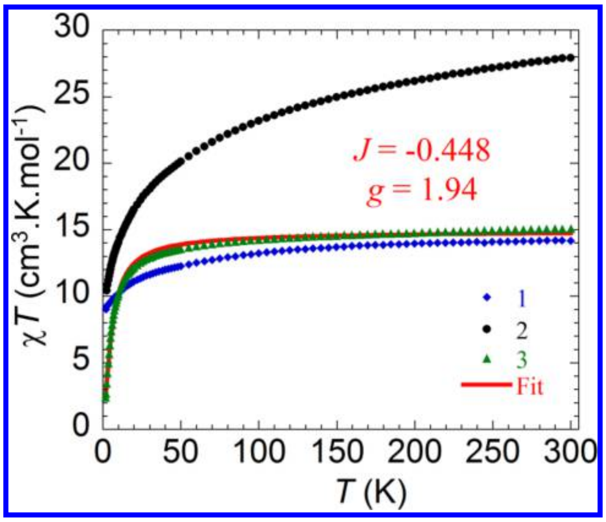

**Figure 3.** Temperature dependence of the $\chi T$ product at 1000 Oe for complexes **1** (◆), **2** (●), and **3** (▲), with $\chi$ being the molar susceptibility per mono- and dinuclear complex defined as $M/H$.

theoretical value of 14.17 cm$^3$ K mol$^{-1}$ for a mononuclear Dy$^{\mathrm{III}}$ complex. Similarly, for **2** and **3**, the respective room temperature $\chi T$ values of 27.92 and 15.08 cm$^3$ K mol$^{-1}$ are also in close agreement with the expected theoretical values of 28.34 and 15.76 cm$^3$ K mol$^{-1}$ for two noninteracting Dy$^{\mathrm{III}}$ ($^6H_{15/2}$, $S = 5/2$, $L = 5$, $g = 4/3$) and Gd$^{\mathrm{III}}$ ($^8S_{7/2}$, $S = 7/2$, $L = 0$, $g = 2$) ions. For **1** and **2**, the $\chi T$ value gradually decreases from the room temperature value with a faster decrease below 50 K to minimum values of 9.22 and 10.42 cm$^3$ K mol$^{-1}$ at 2 K, respectively. This behavior could originate from a combination of the large inherent magnetic anisotropy in Dy$^{\mathrm{III}}$ ions, and the depopulation of the excited states for both complexes. The observed steeper decrease for **2** below 50 K indicates a non-negligible contribution from antiferromagnetic interactions between metal centers. Although such interactions are hard to quantify between highly anisotropic Dy$^{\mathrm{III}}$ ions, such antiferromagnetic interactions are expected to be non-negligible due to the presence of eight occupied orbitals of the central COT″ dianionic ligand acting as a superexchange pathway in **2** as well as the weak direct Dy$^{\mathrm{III}}$−Dy$^{\mathrm{III}}$ covalent interaction with the bond order of 0.04. For complex **3**, the $\chi T$ product remains relatively constant up to 50 K and then decreases sharply to reach 2.4 cm$^3$ K mol$^{-1}$ at 1.8 K. Such behavior in the isotropic Gd$^{\mathrm{III}}$ system indicates the final decrease is primarily due to antiferromagnetic coupling between the metal centers. To quantify the strength of this interaction, application of the Van Vleck equation to the Kambe's vector coupling method was done using the isotropic spin Hamiltonian $H = -JS_a \cdot S_b$ with $S_a = S_b = 7/2$, which was used to fit the variation of $\chi T$ versus $T$. The best-fit parameters obtained are $J = -0.448(1)$ cm$^{-1}$ and $g = 2.00(0)$. Although this $J$ value is relatively small, we have recently demonstrated even much smaller coupling leads to significant effects on relaxation mechanisms.[1h,i] Moreover, it is important to note this value is larger than the obtained value of −0.178(1) cm$^{-1}$ for our previously reported phenoxide bridged dinuclear Gd$_2$ complex with a much shorter Gd$^{\mathrm{III}}$−Gd$^{\mathrm{III}}$ distance (3.82 Å vs 4.21 Å for **3**). Fukuda and co-workers recently demonstrated the $f$−$f$ interactions are non-negligible even at distances of 6.8 Å.[13] Here, the observed intermolecular Dy$^{\mathrm{III}}$−Dy$^{\mathrm{III}}$ distances of 10.39 Å (for **1**), 9.2 Å (for **2**), and 9.03 Å (for **3**) are much larger. Therefore, it is reasonable to assume the intramolecular antiferromagnetic interactions play a significant part in the negative deviation of the $\chi T$ product for **2** and **3**. This illustrates the interaction through the delocalized $\pi$ cloud, and weak direct Ln$^{\mathrm{III}}$−Ln$^{\mathrm{III}}$ covalent interactions are significant.

The $M$ versus $H$ data (Figures S15, S17) below 8 K demonstrate a rapid increase in the magnetization at low magnetic fields for **1**, **2**. For complex **1** at higher fields, $M$ increases linearly at 2 K reaching 5.75 $\mu_B$ under 7 T without saturation. Similar behavior is observed for **2** at high fields where at 2.5 K $M$ increases near linearly reaching 9.18 $\mu_B$ under 7 T without saturation. The $M$ versus $H/T$ data (Figures S16, S18) for both **1** and **2** at high fields does not saturate or overlay onto a single master curve. This indicates the presence of large magnetic anisotropy and/or low-lying excited states in **1** and **2**, which is often seen in Dy$^{\mathrm{III}}$-based systems.[23] In comparison, below 8 K a less steep decrease was observed in the magnetization at low magnetic fields (<2000 Oe) for complex **3** (Figure S19). Above this field, a rapid increase was observed with close to a near saturation value of 12.1 $\mu_B$ at 1.8 K. The non-superimposition of $M$ versus $H/T$ data (Figure S19) for this isotropic system likely arises from low lying excited states. It is important to note the s-shaped magnetization curves at low field further confirm significant interactions between metal ions within the molecule.

To probe any SIM behavior of **1**, both frequency- and temperature-dependent alternating current (ac) magnetic susceptibility measurements were carried out. The data reveal a strong temperature- and frequency-dependent in-phase ($\chi'$) and of the out-of-phase ($\chi''$) magnetic susceptibility under zero applied dc field and 3 Oe ac field below 15 K (Figures 4, 5, S21, S22). In the temperature-dependent $\chi''$ data (Figure 4), a frequency-dependent full peak can be observed along with a tail at lower temperatures. This slow relaxation of the magnetization behavior is indicative of a SIM with a quantum tunneling regime below 5 K. Similarly, the frequency-dependent data in the temperature range of 4.5−9 K display that the intensity of the $\chi''$ increases with decreasing temperature and frequency (Figure 5). Such slow relaxation of the magnetization is indicative of SIM behavior. Between 2 and 4.5 K, a full peak

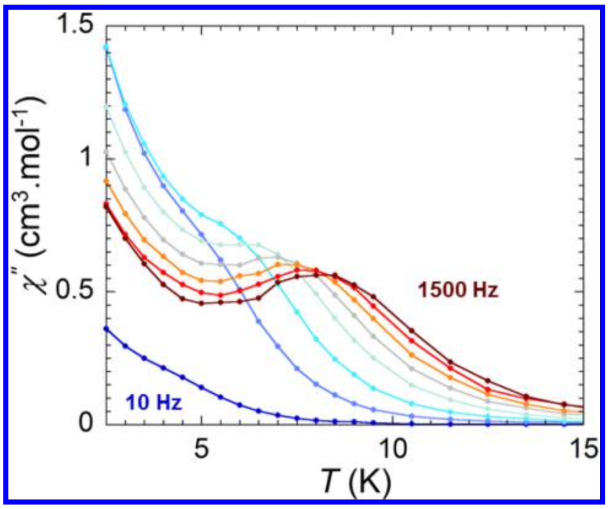

**Figure 4.** Out-of-phase susceptibility ($\chi''$) versus temperature ($T$) for **1** between 10 and 1500 Hz at 0 dc field.

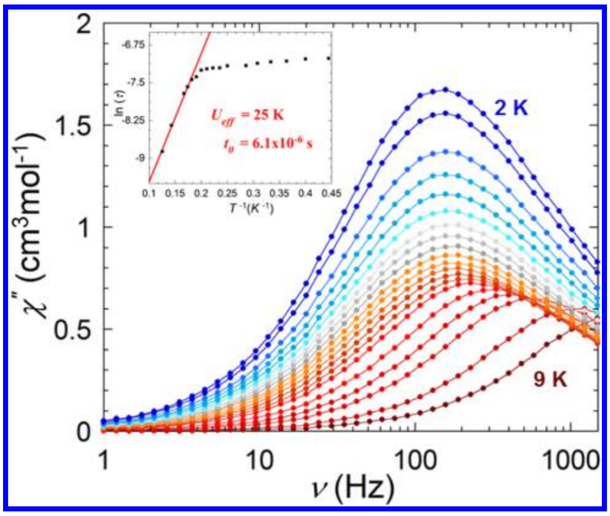

**Figure 5.** Out-of-phase susceptibility ($\chi''$) versus frequency ($\nu$) for **1** in the temperature range 2.5−9 K at 0 dc field. Inset: Plots of ln($\tau$) versus $T$ for **1**. The solid lines represent the Arrhenius fit of the frequency-dependent data.

is observed, but there is no frequency dependence of the $\chi''$, confirming the quantum tunneling of the magnetization (QTM) for **1** under zero dc field. The anisotropic barrier was determined, $U_{\mathrm{eff}} = 25$ K, $\tau_0 = 6 \times 10^{-6}$ s, calculated from the Arrhenius equation ($\tau = \tau_0 \exp(U_{\mathrm{eff}}/kT)$), and this relatively small barrier is expected due to the presence of significant QTM (Figure 5, inset). Our recent studies on a related [Dy $^{\mathrm{III}}$(COT″)$_2$Li(THF)(DME)][8] exhibited similar frequency-dependent behavior in the same temperature range with $U_{\mathrm{eff}} = 18$ K, $\tau_0 = 6 \times 10^{-6}$ s under 0 dc field.

This reported Li-bound mononuclear sandwich molecule was also found to have unusual relaxation dynamics where multiple field-dependent relaxation processes were observed.[8] We performed field-dependent studies to elucidate whether similar relaxation dynamics are inherent to **1**. In the plot of $\chi''$ versus $\nu$ (Figure S23, top) at 3 K, the peak with a maximum at 110 Hz under 0 Oe dc field decreases and slightly shifts right under a 200 Oe dc field. Also, under a 200 Oe applied dc field, a secondary tail appears at low frequency. Under applied dc fields over 300 Oe, the initial peak at 110 Hz disappears completely, leaving only a tail at low frequency. Such relaxation dynamics are nearly identical to those observed with the Li-bound monomer.[8] This suggests that the presence of the Li bound to the COT″ ring has a slight effect on the relaxation dynamics of the Dy$^{\mathrm{III}}$−COT″ sandwich complex due to structural distortions.

To probe the SMM behavior of **2**, both temperature- and frequency-dependent ac magnetic susceptibility measurements were carried out. Under zero applied dc field and 3 Oe ac field oscillating at frequencies between 1 and 1500 Hz, temperature-dependent measurements exhibit an out-of phase ($\chi''$) signal below 15 K in the $\chi''$ versus $T$ plot (Figure S24). Above 1000 Hz, the observation of broad shoulders signals the possibility of overlapping multiple relaxation modes occurring in **2**. As a means to further elucidate this phenomenon, Figure S25 depicts the frequency-dependent studies under a zero static dc field between 2.5 and 9 K and plotted as $\chi''$ versus $\nu$. Observation of shifting peak maxima under 5 K indicates SMM behavior. From the Arrhenius equation ($\tau = \tau_0 \exp(U_{\mathrm{eff}}/kT)$), the calculated anisotropic barrier is $U_{\mathrm{eff}} = 9$ K, $\tau_0 = 1.8 \times 10^{-5}$ s (Figure S26).

The absence of a clear full peak in the $\chi''$ versus $T$ plot suggests the presence of QTM. As a result of applying an optimum static dc field of 600 Oe (Figure S23, bottom) to reduce QTM (Figures 6, 7, S27, S28), Figures 6 and 7 reveal a frequency- and temperature-dependent out-of-phase ($\chi''$) signal with shifting peak maxima toward higher temperatures. The absence of overlapping peak maxima at low temperatures (Figure 7) suggests the lack of a quantum regime; thus QTM is minimized upon application of the static dc field. In the $\chi''$ versus $T$ plot, the occurrence of broad peaks spanning from 2.5 to 11 K above 500 Hz signals the possibility of frequency-dependent multiple relaxation processes in **2**. Figure 6 insert displays the three proposed relaxation mechanisms. From the Arrhenius equation, the calculated anisotropic barriers for the

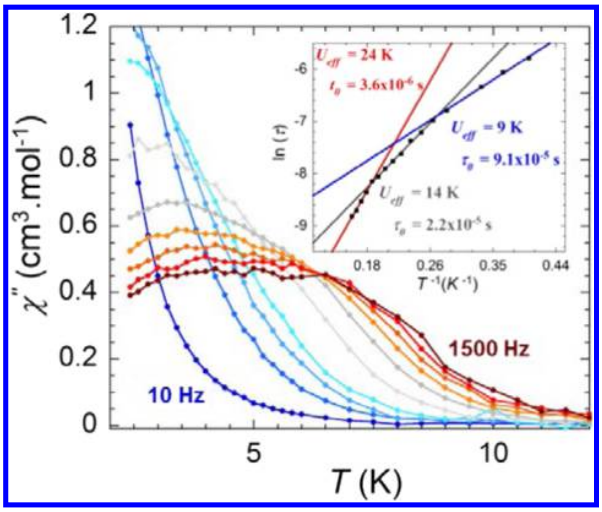

**Figure 6.** Temperature dependence of the out-of-phase susceptibility ($\chi''$) plot of **2** between 10 and 1500 Hz under an optimal applied dc field of 600 Oe. Inset: Plots of ln($\tau$) versus $T$ for **2** at $H_{\mathrm{dc}} = 600$ Oe. The solid lines represent the Arrhenius fit of the frequency-dependent data.

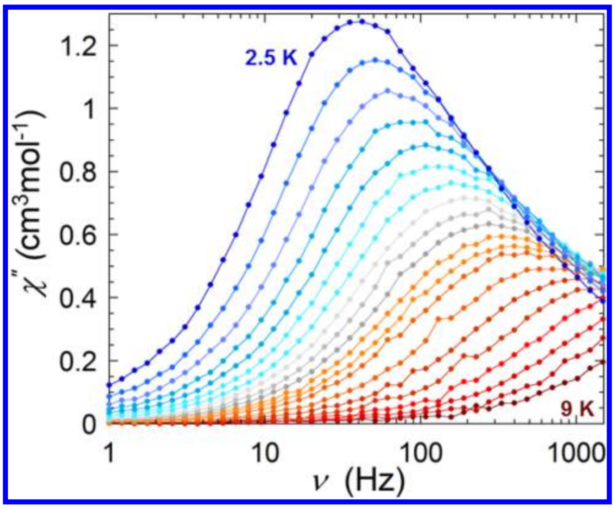

**Figure 7.** Out-of-phase susceptibility ($\chi''$) versus frequency ($\nu$) for **2** in the temperature range 2.5−9 K under an optimum applied dc field of 600 Oe.

observed activated regimes are (A) $U_{\text{eff}} = 24$ K ($\tau_0 = 3.6 \times 10^{-6}$ s), (B) $U_{\text{eff}} = 19$ K ($\tau_0 = 2.2 \times 10^{-5}$ s), and (C) $U_{\text{eff}} = 9$ K ($\tau_0 = 9.1 \times 10^{-5}$ s). The unsaturated curve confirms the reduction of QTM in **2** under the applied optimum dc field. The presence of multiple relaxation barriers was further explored using a graphical representation, $\chi'$ versus $\chi''$ (Cole−Cole plot), calculated using the generalized Debye model[24] in a temperature range of 2.5−9 K (Figure S29). Unsymmetrical semicircles were poorly fit with $\alpha$ values ranging from 0.04 to 0.35, indicating high amounts of disorder and relaxation times not unique to a single relaxation mechanism. A good fit did occur at 5.5 K with $\alpha = 0.04$, suggesting one relaxation pathway may be favored at this temperature. In the case of **3**, no ac signal was observed as expected for an isotropic system precluding any SMM behavior.

From our studies of the mononuclear precursor building block unit, **1**, exhibiting intricate multiple relaxation modes, it is not surprising that the relaxation dynamics of **2** are not unique to a single relaxation mechanism. Hence, coupling two SIM units through central COT″ ligand to create an SMM further promotes the overlap of several relaxation pathways, and the observed complex features are expected.

### 3.5. Calculation of Magnetic Anisotropic Axes.

To probe the magnetic anisotropic axes of **1** and **2**, the low-lying electronic levels (Kramers doublets) on the $\text{Dy}^{\text{III}}$ sites have been calculated by ab initio with the MOLCAS7.6 package[29] in different structural and basis set approximations (Table S1). The energies of the eight Kramers doublets arising from the $J = 15/2$ atomic ground multiplet of $\text{Dy}^{\text{III}}$ are given in Table S2. The calculation of the magnetic properties of each Kramers doublet has been done with SINGLE_ANISO module.[25,26] The results for the main values of the obtained $g$ tensors are given in Table S2. The directions of main magnetic axes on the $\text{Dy}^{\text{III}}$ sites of **1** and **2** are shown in Figure S30 and Figure 8a, respectively. We can see in **2** that the directions of the local magnetic axes are far from the axis connecting the two dysprosium ions. This proves the strong effect on the distant silyl groups on the direction of anisotropy axis. This is in line with direction of the anisotropic axis observed in **1** as well as in previous findings where there was a strong effect of the second coordination sphere on the magnetic anisotropy of strongly anisotropic metal ions in a $\text{Co}^{\text{II}}$ complexes[27] and more recently Sessoli and co-worker's $\text{Dy}^{\text{III}}$ complexes.[28] For comparison, we did similar calculations for the symmetrized structure of **2**, where the silyl groups were replaced by hydrogen and the $\text{Dy}^{\text{III}}$−C groups for each COT were averaged to one distance so as to have the overall symmetry $C_{8h}$ at each $\text{Dy}^{\text{III}}$ site (Figure 8b).

The results for the lowest eight Kramers doublets on each $\text{Dy}^{\text{III}}$ are shown in Table S3. We can see that the ground state $g_Z$ roughly corresponds to $J = 9/2$ contrary to the case of real geometry, where $g_Z$ is closer to $J = 15/2$ (as was found in many other low symmetric $\text{Dy}^{\text{III}}$ complexes).[29] On the other hand, the main magnetic axis on each $\text{Dy}^{\text{III}}$ ion is directed now along the symmetry axis of the complex.

To get more insight into the obtained spectrum of crystal field levels on each Dy site (Table S2), we calculated the crystal field parameters describing the splitting of $J = 15/2$ ground atomic multiplet with SINGLE_ANISO module of MOLCAS. The results are given in Table S4 for the quantization axis taken along $\text{Dy}^{\text{III}}$−$\text{Dy}^{\text{III}}$. We can see that all $B_n^{\ 0}$ parameters are positive, which means that the equatorial component of the ligand field is stronger than the axial one. This will lead to the stabilization of the lowest possible momentum projection ($m = \pm 1/2$) if all $B_n^{\ m} = 0$ for $m \neq 0$, because it corresponds to a prolate distribution of 4*f* electron charge density in the case of $\text{Dy}^{\text{III}}$.[30] In our case, however, all 27 parameters $B_n^{\ m}$ are nonzero (see Table S4) because of the lack of rotational symmetry around the chosen quantization axis (Figure 8a). As a result, the lowest Kramers doublet on $\text{Dy}^{\text{III}}$ sites will correspond to a combination of several projections $m$. On the other hand, the predominant equatorial ligand field of the two COT ligands will strongly destabilize the doublet with highest moment $J = \pm 15/2$, because it corresponds to an oblate charge density distribution in $\text{Dy}^{\text{III}}$.[30] This is confirmed by our ab initio calculations (Table S2).

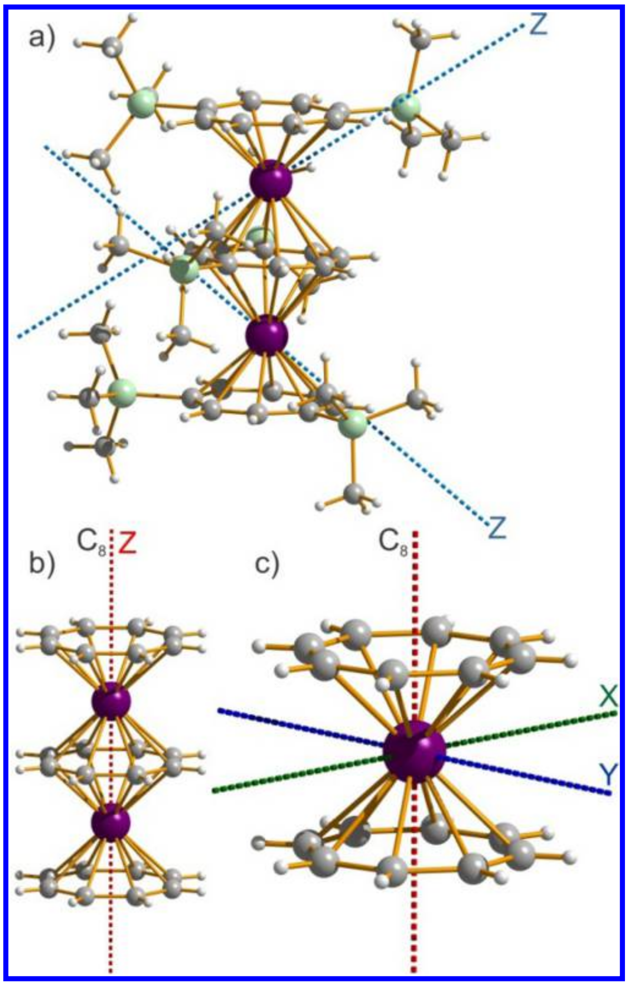

**Figure 8.** Orientation of the main magnetic axes of the ground Kramers doublets on Dy centers of (a) the initial complex **2**; (b) the symmetrized **2**; and (c) the symmetrized **1**.

For the directions of local anisotropy axes as shown in Figure 8a and for the calculated $g$ factors (Table S2), the dipolar interaction between magnetic moment on $\text{Dy}^{\text{III}}$ is rather weak albeit antiferromagnetic. The calculated splitting of the exchange doublets in $\text{Dy}_2\text{COT}_3$ due to this interaction only amounts to 1.3 $\text{cm}^{-1}$. This means that, contrary to the usual situation, the main contribution to the magnetic interaction between $\text{Dy}^{\text{III}}$ ions comes from anisotropic exchange interaction, which is expected to be relatively large on the basis of DFT calculations discussed above.

Finally, we considered one single symmetric $[Dy^{III}(COT)_2]$ unit (Figure 8c). The results of the calculations are shown in Table S3. Surprisingly, the ground Kramers doublet corresponds in this case to $J = 1/2$ as expected and is of easy plane type (Table S3). The directions of the main magnetic axes are shown in Figure 8c. This shows once more how sensitive the magnetic properties of the $Ln^{III}$ ions are to changes in the second and more distant coordination spheres. We may conclude that for the complexes of $[Dy^{III}_2(COT'')_3]$ type, the obtained large magnetic moment on the $Dy^{III}$ ions in the ground state is due to the low symmetry environment. The analysis of the magnetic anisotropy of local Kramers doublets shows that the highest one (KD 8 in Table S3) is very axial. This suggests that a replacement of $Dy^{III}$ by $Er^{III}$ in **1** might result in a strong SMM effect of the complex. The same is true for the $[Dy^{III}(COT)_2]$ in Figure 8c: according to Table S3, the replacement of $Dy^{III}$ with $Er^{III}$ should also enhance the SMM behavior of this complex. With these findings in mind, we are currently exploring several synthetic strategies to isolate the unsilylated analogues of **1** and **2**.

## 4. CONCLUSION

A unique organometallic building block approach was successfully employed to create two dinuclear triple-decker lanthanide complexes. The use of planar $COT''^{2-}$ ligands allows for access to a new coordination environment that provides a unique ligand field around the spin carrier. As such, isolated complexes **1** and **2** act as an SIM and SMM, respectively, in a unique ligand system. Isotropic analogous complex **3** provided further evidence of the strength and nature of intramolecular coupling in the dinulcear triple-decker complex. In contrast to typical lanthanide complexes with weak metal−ligand covalencies, the electronic structure analysis of these $Dy^{III}$ complexes demonstrates high metal−ligand covalency. This methodology allows us to promote a delocalized superexchange pathway for magnetic interactions. Evidence of a non-negligible superexchange interaction via the central $COT''^{2-}$ ligand was observed through magnetic measurements as well as through DFT calculation. Surprisingly, a weak direct $Dy^{III}-Dy^{III}$ covalent interaction was also observed. In addition, ab initio calculations reveal the importance of the second coordination sphere on the magnetic properties. Trimethylsilyl groups on the $COT''^{2-}$ ligand significantly influence the orientation of the magnetic axis, while the absence of these groups led to perfect alignment of the anisotropy axis along the idealized $C_8$ axis of the dinuclear molecule. This in theory should enhance the overall magnetic anisotropy of the dinuclear molecule by promoting further coupling (due to the reduction of the steric hindrance brought by trimthylsilyl groups), thus yielding larger energy barrier SMMs. The above findings lend credence to the extended use of the building block methodology toward larger linear multimetallic systems such as single-chain magnets, which could potentially lead to significantly larger energy barrier SMMs.

## ■ ASSOCIATED CONTENT

### Ⓢ Supporting Information

Complete experimental and computational details, and cif files. This material is available free of charge via the Internet at http://pubs.acs.org.

## ■ AUTHOR INFORMATION

### Corresponding Author

m.murugesu@uottawa.ca

### Notes

The authors declare no competing financial interest.

## ■ ACKNOWLEDGMENTS

We thank the University of Ottawa, NSERC (Discovery and RTI grants), CFI for their financial support. L.U. is a postdoc of the FWO-Vlanderen and also gratefully acknowledges the financial support from the Methusalem and INPAC grants of the KU Leuven.

## ■ REFERENCES

(1) (a) Christou, G.; Gatteschi, D.; Hendrickson, D. N.; Sessoli, R. *MRS Bull.* **2000**, *25*, 66. (b) Bogani, L.; Wernsdorfer, W. *Nat. Mater.* **2008**, *7*, 179. (c) Coronado, E.; Day, P. *Chem. Rev.* **2004**, *104*, 5419. (d) Thomas, L.; Lionti, L.; Ballou, R.; Gatteschi, D.; Sessoli, R.; Barbara, B. *Nature* **1996**, *383*, 145. (e) Sokol, J. J.; Hee, A. G.; Long, J. R. *J. Am. Chem. Soc.* **2002**, *124*, 7656. (f) Maheswaran, S.; Chastanet, G.; Teat, S. J.; Mallah, T.; Sessoli, R.; Wernsdorfer, W.; Winpenny, R. E. P. *Angew. Chem. Int. Ed.* **2005**, *44*, 5044. (g) Zaleski, C. M.; Depperman, E. C.; Kampf, J. W.; Kirk, M. L.; Pecoraro, V. L. *Angew. Chem. Int. Ed.* **2004**, *43*, 3912. (h) Long, J.; Habib, F.; Lin, P. -H.; Korobkov, I.; Enright, G.; Ungur, L.; Wernsdorfer, W.; Chibotaru, L. F.; Murugesu, M. *J. Am. Chem. Soc.* **2011**, *133*, 5319. (i) Habib, F.; Lin, P.-H.; Long, J.; Korobkov, I.; Wernsdorfer, W.; Murugesu, M. *J. Am. Chem. Soc.* **2011**, *133*, 8830. (j) Williams, U. J.; Mahoney, B. D.; DeGregorio, P. T.; Carroll, P. J.; Nakamaru-Ogiso, E.; Kikkawa, J. M.; Schelter, E. J. *Chem. Commun.* **2012**, *48*, 5593.

(2) (a) Ishikawa, N.; Sugita, M.; Ishikawa, T.; Koshihara, S.; Kaiz, Y. *J. Am. Chem. Soc.* **2003**, *125*, 8694. (b) Magnani, N.; Apostolidis, C.; Morgenstern, A.; Colineau, E.; Griveau, J. C.; Bolvin, H.; Walter, O.; Caciuffo, R. *Angew. Chem. Int. Ed.* **2011**, *50*, 1696. (c) Jiang, S.-D.; Wang, B.-W.; Sun, H.-L.; Wang, Z.-M.; Gao, S. *J. Am. Chem. Soc.* **2011**, *133*, 4730. (d) Li, D.-P.; Wang, T.-W.; Li, C.-H.; Lin, D.-S.; Li, Y.-Z.; You, X.-Z. *Chem. Commun.* **2010**, *46*, 2929. (e) Aldamen, M. A.; Clemente-Juan, J. M.; Coronado, E.; Marti-Gastaldo, C.; Gaita-Arino, A. *J. Am. Chem. Soc.* **2008**, *130*, 8874.

(3) (a) Blagg, R. J.; Muryn, C. A.; McInnes, E. J. L.; Tuna, F.; Winpenny, R. E. P. *Angew. Chem. Int. Ed.* **2011**, *50*, 6530. (b) Lin, P.-H.; Burchell, T. J.; Murugesu, M. *Angew. Chem. Int. Ed.* **2009**, *48*, 9489. (c) Rinehart, J. D.; Fang, M.; Evans, W. J.; Long, J. R. *J. Am. Chem. Soc.* **2011**, *133*, 14236.

(4) (a) Ako, A. M.; Hewitt, I. J.; Mereacre, V.; Clerac, R.; Wernsdorfer, W.; Anson, C. E.; Powell, A. K. *Angew. Chem. Int. Ed.* **2006**, *45*, 4926. (b) Murugesu, M.; Habrych, M.; Wernsdorfer, W.; Abboud, K. A.; Christou, G. *J. Am. Chem. Soc.* **2004**, *126*, 4766. (c) Milios, C. J.; Vinslava, A.; Wernsdorfer, W.; Prescimone, A.; Wood, P. A.; Parsons, S.; Perlepes, S. P.; Christou, G.; Brechin, E. K. *J. Am. Chem. Soc.* **2007**, *129*, 6547.

(5) (a) Winpenny, R. E. P. *J. Chem. Soc., Dalton Trans.* **2002**, 1 and references therein. (b) Woodruff, D. N.; Tuna, F.; Bodensteiner, M.; Winpenny, R. E. P.; Layfield, R. A. *Organometallics* **2012**, DOI: 10.1021/om3010096.

(6) (a) Glaser, T. *Chem. Commun.* **2011**, *47*, 116. (b) Freedman, D. E.; Jenkins, D. M.; Iavorone, A. T.; Long, J. R. *J. Am. Chem. Soc.* **2008**, *130*, 2884. (c) Karada, F.; Shatruk, M.; Perez, L. M.; Dunbar, K. R. *Chem.-Eur. J.* **2010**, *16*, 7164. (d) Long, J.; Chamoreau, L. M.; Marvaud, V. *Dalton Trans.* **2010**, *39*, 593.

(7) (a) Jeletic, M.; Perras, F.; Gorelsky, S.; Le Roy, J.; Korobkov, I.; Bryce, D.; Murugesu, M. *Dalton Trans.* **2012**, *41*, 8060. (b) Burton, N. C.; Cloke, F. G. N.; Joseph, S. C. P.; Karamallakis, H.; Sameh, A. A. *J. Organomet. Chem.* **1993**, 462. (c) Burton, N. C.; Cloke, F. G. N.; Hitchcock, P. B.; de Lemos, H. C.; Sameh, A. A. *J. Chem. Soc.* **1989**, 1462.

(8) Jeletic, M.; Lin, P.-H.; Le Roy, J. J.; Korobkov, I.; Gorelsky, S. I.; Murugesu, M. *J. Am. Chem. Soc.* **2011**, *133*, 19286.

(9) Sheldrick, G. M. *SADABS — Bruker AXS area detector scaling and absorption, version 2008/1*; University of Göttingen: Germany, 2008.

(10) Sheldrick, G. M. *Acta Crystallogr.* **2008**, *A64*, 112.

(11) Frisch, M. J.; Trucks, G. W.; Schlegel, H. B.; Scuseria, G. E.; Robb, M. A.; Cheeseman, J. R.; Scalmani, G.; Barone, V.; Mennucci, B.; Petersson, G. A.; Nakatsuji, H.; Caricato, M.; Li, X.; Hratchian, H. P.; Izmaylov, A. F.; Bloino, J.; Zheng, G.; Sonnenberg, J. L.; Hada, M.; Ehara, M.; Toyota, K.; Fukuda, R.; Hasegawa, J.; Ishida, M.; Nakajima, T.; Honda, Y.; Kitao, O.; Nakai, H.; Vreven, T.; Montgomery, J. A., Jr.; Peralta, J. E.; Ogliaro, F.; Bearpark, M.; Heyd, J. J.; Brothers, E.; Kudin, K. N.; Staroverov, V. N.; Kobayashi, R.; Normand, J.; Raghavachari, K.; Rendell, A.; Burant, J. C.; Iyengar, S. S.; Tomasi, J.; Cossi, M.; Rega, N.; Millam, J. M.; Klene, M.; Knox, J. E.; Cross, J. B.; Bakken, V.; Adamo, C.; Jaramillo, J.; Gomperts, R.; Stratmann, R. E.; Yazyev, O.; Austin, A. J.; Cammi, R.; Pomelli, C.; Ochterski, J. W.; Martin, R. L.; Morokuma, K.; Zakrzewski, V. G.; Voth, G. A.; Salvador, P.; Dannenberg, J. J.; Dapprich, S.; Daniels, A. D.; Farkas, Ã.; Foresman, J. B.; Ortiz, J. V.; Cioslowski, J.; Fox, D. J. *Gaussian 09*, revision A.02; Gaussian, Inc.: Wallingford, CT, 2009.

(12) Noodleman, L. *J. Chem. Phys.* **1981**, *74*, 5737.

(13) (a) Gorelsky, S. I. *AOMix – Software for Electronic Structure Analysis; Centre for Catalysis Research and Innovation, Department of Chemistry*; University of Ottawa: Ottawa, ON, 2012; http://www.sg-chem.net. (b) Gorelsky, S. I.; Lever, A. B. P. *J. Organomet. Chem.* **2001**, *635*, 187.

(14) Schafer, A.; Huber, C.; Ahlrichs, R. *J. Chem. Phys.* **1994**, *100*, 5829.

(15) (a) Dolg, M.; Stoll, H.; Preuss, H. *Theor. Chem. Acc.* **1993**, *85*, 441. (b) Cao, X. Y.; Dolg, M. *J. Chem. Phys.* **2001**, *115*, 7348. (c) Cao, X. Y.; Dolg, M. *J. Mol. Struct. (THEOCHEM)* **2002**, *581*, 139.

(16) (a) Becke, A. D. *J. Chem. Phys.* **1993**, *98*, 5648. (b) Lee, C.; Yang, W.; Parr, R. G. *Phys. Rev. B* **1988**, *37*, 785.

(17) (a) Mayer, I. *Int. J. Quantum Chem.* **1986**, *29*, 73. (b) Gorelsky, S. I.; Basumallick, L.; Vura-Weis, J.; Sarangi, R.; Hedman, B.; Hodgson, K. O.; Fujisawa, K.; Solomon, E. I. *Inorg. Chem.* **2005**, *44*, 4947.

(18) Gorelsky, S. I.; Solomon, E. I. *Theor. Chem. Acc.* **2008**, *129*, 57.

(19) Mulliken, R. S. *J. Chem. Phys.* **1955**, *23*, 1833.

(20) (a) Meermann, C.; Ohno, K..; Törnroos, K. W.; Mashima, K.; Anwander, R. *Eur. J. Inorg. Chem.* **2009**, *1*, 76. (b) Walter, M. D.; Booth, C. H.; Lukens, W. W.; Andersen, R. A. *Organometallics* **2009**, *28*, 698.

(21) (a) Poremba, P.; Reissmann, U.; Noltmeyer, M.; Schmidt, H.-G.; Brüser, W.; Edelmann, F. T. *J. Organomet. Chem.* **1997**, *554*, 1. (b) Edelmann, A.; Blaurock, S.; Lorenz, V.; Hilfert, L.; Edelmann, F. T. *Angew. Chem. Int. Ed.* **2007**, *46*, 6732. (c) Lorenz, V.; Edelmann, A.; Blaurock, S.; Freise, F.; Edelmann, F. T. *Organometallics* **2007**, *26*, 6681. (d) Poremba, P.; Edelmann, F. T. *J. Organomet. Chem.* **1998**, *553*, 393. (e) Lorenz, V.; Blaurock, S.; Hrib, C. G.; Edelmann, F. T. *Organometallics* **2010**, *29*, 4787.

(22) Beck, V.; O'Hare, D. *J. Organomet. Chem.* **2004**, *689*, 3920.

(23) (a) Yan, P.-F.; Lin, P.-H.; Habib, F.; Aharen, T.; Murugesu, M.; Deng, Z.-P.; Li, G.-M.; Sun, W.-B. *Inorg. Chem.* **2011**, *50*, 7059. (b) Savard, D.; Lin, P.-H.; Burchell, T. J.; Korobkov, I.; Wernsdorfer, W.; Clerac, R.; Murugesu, M. *Inorg. Chem.* **2009**, *48*, 11748. (c) Lin, P.-H.; Korobkov, I.; Wernsdorfer, W.; Ungar, L.; Chibotaru, L. F.; Murugesu, M. *Eur. J. Inorg. Chem.* **2011**, 1535. (d) Lin, P.-H.; Gorelsky, S. I.; Savard, D.; Burchell, T. J.; Wernsdorfer, W.; Murugesu, M. *Dalton Trans.* **2010**, *39*, 7650. (e) Burrow, C. E.; Burchell, T. J.; Lin, P.-H.; Habib, F.; Wernsdorfer, W.; Clerac, R.; Murugesu, M. *Inorg. Chem.* **2009**, *48*, 8051. (f) Lin, P.-H.; Burchell, T. J.; Clerac, R.; Murugesu, M. *Angew. Chem. Int. Ed.* **2008**, *47*, 8848.

(24) Gattsechi, D.; Sessoli, R.; Villain, J. *Molecular Nonomagnets*; Oxford University Press: New York, 2006; and references therein.

(25) Aquilante, F.; De Vico, L.; Ferré, N.; Ghigo, G.; Malmqvist, P.-Å.; Neogrády, P.; Pedersen, T. B.; Pitoňák, M.; Reiher, M.; Roos, B. O.; Serrano-Andrés, L.; Urban, M.; Veryazov, V.; Lindh, R. *J. Comput. Chem.* **2010**, *31*, 224.

(26) Chibotaru, L. F.; Ungur, L. *J. Chem. Phys.* **2012**, *137*, 064112.

(27) Petit, S.; Pilet, G.; Luneau, D.; Chibotaru, L. F.; Ungur, L. *Dalton Trans.* **2007**, *40*, 4582.

(28) Cucinotta, G.; Perfetti, M.; Luzon, J.; Etienne, M.; Car, P.-E.; Caneschi, A.; Calvez, G.; Bernot, K.; Sessoli, R. *Angew. Chem. Int. Ed.* **2012**, *51*, 1606.

(29) Ungur, L.; Chibotaru, L. F. *Phys. Chem. Chem. Phys.* **2011**, *13*, 20086.

(30) Rinehart, J. D.; Long, J. R. *Chem. Sci.* **2011**, *2*, 2078.